Supplementary Information

Deciphering carbon–sulfur rotational distribution in a crystalline host for enhanced red persistent organic phosphorescence

Sakuya Ueda, Kazuki Fujita, Bahadur Sk and *Shuzo Hirata**

Department of Engineering Science, The University of Electro-Communications, 1-5-1, Chofugaoka, Chofu, Tokyo 182-8585, Japan

*Corresponding author. E-mail: shuzohirata@uec.ac.jp

This file includes

1. Synthesis of chromophores and characterization (Figure S1-S4)

Synthesized chromophores were characterized via proton nuclear magnetic resonance (^{1}H NMR), carbon nuclear magnetic resonance (^{13}C NMR) (ECA-500, JEOL, Tokyo, Japan) spectroscopy, matrix-assisted laser-desorption ionization high-resolution mass spectrometry (HRMS-MALDI) (JMS-S3000, JEOL), and elemental analysis (Series II CHNS/O 2400 analyzer, PerkinElmer, MA, USA). Detailed information regarding the synthesis, purification and characterizations is as follows.

Dibenzo[*g,p*]chrysen-2-yl(phenyl)methanone (2h):

Dibenzo[g,p]chrysene (102 mg, 0.311 mmol, 1.0 equiv.) and anhydrous aluminum chloride (62.7 mg, 0.470 mmol, 1.5 equiv.) were dissolved in dichloromethane (4.0 mL) under a nitrogen atmosphere. Next, 2.0 mL of a solution of benzyl chloride (0.1 mL) in dichloromethane (3.8 mL) was added dropwise under a nitrogen atmosphere at 0°C and stirred. After the mixture was allowed to react at room temperature (RT) for 3.5 h, an excess amount of 1 M hydrogen chloride (HCl) was added to terminate the reaction. After the remaining HCl was quenched with saturated sodium hydrogen carbonate, the organic phase was washed with H_2O and dichloromethane 3 times, dried over sodium sulfate (Na_2SO_4), and then filtered to give a crude material. The crude material was purified by column chromatography (silica gel; eluent = 30 % dichloromethane/hexane) to give **2h** (104 mg, 77%) as a paled yellow powder. Furthermore, high-purified **2h** was obtained by sublimation purification. ^{1}H NMR ($CDCl_3$, 500MHz): δ (ppm) 9.18(d, J = 1.5Hz, 1H), 8.79 (d, J = 8.5 Hz, 1H), 8.68-8.74 (m, 6H), 8.06 (dd, J = 8.5 Hz, J = 1.5 Hz, 1H), 7.97 (d, J = 8.5 Hz, 2H), 7.65-7.74 (m, 7H), 7.57 (t, J = 8.0 Hz, 2H) (Fig. S1a). ^{13}C NMR ($CDCl_3$, 125MHz): δ (ppm) 196.51, 137.97, 134.89, 132.49, 131.94, 131.31, 130.93,

130.83, 130.21, 129.47, 129.37, 129.11, 129.07, 129.04, 128.99, 128.83, 128.67, 128.44, 127.32, 127.22, 127.13, 127.00, 126.96, 126.92, 126.86, 126.76, 126.38, 123.75, 123.70 (Fig. S1b). HRMS-MALDI TOF (m/Z): [M]+ calculated for $C_{33}H_{20}O$, 432.15133; Found, 432.15087 (Fig. S1c). Analysis calculated for $C_{33}H_{20}O$: C, 91.64; H, 4.66. Found C, 91.51; H, 4.49.

2-Bromodibenzo[*g,p*]chrysene:

Chromophore **1h** (199 mg, 0.607 mmol, 1.0 equiv.) was dissolved in chlorobenzene (11.78 mL). After a mixture of bromine (0.100 mL, 0.593 mmol, 0.98 equiv.) in chlorobenzene (5.00 mL) was prepared, 1.56 mL of the solution was added dropwise to the chlorobenzene solution in which **1h** had been dissolved. The mixture was reacted for 43 h at 110°C under a nitrogen atmosphere. After chloroform was added, the organic phase was washed with H_2O 3 times, dried over Na_2SO_4, and then filtered to give a crude material. The crude material was purified by column chromatography (silica gel; eluent = 10 % dichloromethane/hexane) to give 2-bromodibenzo[*g,p*]chrysene (170 mg, 69%) as a white powder.[S1]

Dibenzo[*g,p*]chrysen-2-yl(phenyl)sulfane (3h):

2-Bromodibenzo[*g,p*]chrysene (150 mg, 0.368 mmol, 1.0 equiv.), diphenyl disulfide (61.3 mg, 0.281 mmol, 0.76 equiv.), [1,1'-bis(diphenylphosphino)ferrocene]palladium(II) (16.8 mg, 0.0230 mmol, 0.062 equiv.), and zinc (36.5 mg, 0.558 mmol, 1.5 equiv.) were dissolved in 4.5 mL of tetrahydrofuran (THF). The solution was reacted under a nitrogen atmosphere at 70° C. for 24 h. After dichloromethane was added, the organic phase was washed with H_2O 3 times, dried over Na_2SO_4, and then filtered to give a crude material.

The crude material was purified by column chromatography (silica gel; eluent = 10 % dichloromethane/hexane) to give **3h** (99.3 mg, 62%) as a white powder. Furthermore, high-purified **3h** was obtained by sublimation purification. ^{1}H NMR ($CDCl_3$, 500MHz): δ (ppm) 8.67-8.71 (m, 5H), 8.62 (d, *J* = 8.0 Hz, 2H), 8.56 (d, *J* = 10 Hz, 1H), 7.62-7.67 (m, 6H), 7.55 (dd, *J* = 8.5 Hz, *J* = 1.5 Hz, 1H), 7.47 (d, *J* = 7.5 Hz, 2H), 7.36 (t, *J* = 7.5 Hz, 2H), 7.30 (t, *J* = 7.5 Hz, 1H) (Fig. S2a). ^{13}C NMR ($CDCl_3$, 125MHz): δ (ppm) 135.70, 134.11, 131.49, 131.21, 130.89, 130.15, 129.75, 129.49, 129.26, 129.14, 129.03, 129.01, 128.91, 128.85, 128.76, 128.08, 127.71, 127.28, 127.19, 126.90, 126.70, 126.64, 125.86, 123.63, 123.61 (Fig. S2b). HRMS-MALDI TOF (m/Z): [M]+ calculated for $C_{32}H_{20}S$, 436.12802; Found, 436.12774 (Fig. S2c). Analysis calculated for $C_{32}H_{20}S$: C, 88.04; H, 4.62; S, 7.34. Found C, 87.99; H, 4.68; S, 7.58.

Dibenzo[*g,p*]chrysene-d_{16}:

Chromophore **1h** (123 mg) was treated with 10 % Pd on active carbon (125 mg) and D_2O (25 mL) in a 50 mL teflon-lined autoclave at 240 °C for 12 h. The internal pressure reached 4–5 MPa. After slowly cooling to RT, chloroform was added. The organic phase was washed with H_2O 3 times and dried over Na_2SO_4, and then filtered to give a crude material. The crude material was purified by column chromatography (silica gel; eluent = 25 % dichloromethane/hexane) to dibenzo[*g,p*]chrysene-d_{16} (93 mg) as a white powder. MALDI TOF (m/Z): [M]+ calculated for $C_{26}D_{16}$, 344.2256, Found, 334.225. The mass analysis confirmed that sufficient deuterium substitution had been achieved, as shown by the increase in molecular weight distribution in Fig. S3a.

2-Bromodibenzo[*g,p*]chrysene-1,3,4,5,6,7,8,9,10,11,12,13,14,15,16-d_{15}:

The prepared dibenzo[g,p]chrysene-d_{16} (87.9 mg, 0.255 mmol, 1.0 equiv.) was dissolved in chlorobenzene (5.04 mL). After a mixture of bromine (0.10 mL) in chlorobenzene (5.00 mL) was prepared, 0.68 mL of the solution was added dropwise to the chlorobenzene solution in which **1h** had been dissolved. The mixture was reacted for 43 h at 110°C under a nitrogen atmosphere. After chloroform was added, the organic phase was washed with H_2O 3 times, dried over Na_2SO_4, and then filtered to give a crude material. The crude material was purified by column chromatography (silica gel; eluent = 10 % dichloromethane/hexane) to give 2-bromodibenzo[*g,p*]chrysene-1,3,4,5,6,7,8,9,10,11,12,13,14,15,16-d_{15} (70.2 mg, 65%) as a white powder. MALDI TOF (m/Z): [M]+ calculated for $C_{26}D_{15}Br$, 421.1299, Found, 421.129. The mass analysis confirmed that sufficient deuterium substitution had been achieved, as shown by the increase in molecular weight distribution in Fig. S3b.

Dibenzo[*g,p*]chrysen-2-yl(phenyl)sulfane-1,3,4,5,6,7,8,9,10,11,12,13,14,15,16-d_{15} (3d):

2-Bromodibenzo[*g,p*]chrysene-1,3,4,5,6,7,8,9,10,11,12,13,14,15,16-d_{15} (60.6 mg, 0.144 mmol, 1.0 equiv.), diphenyl disulfide (20.5 mg, 0.0938 mmol, 0.65 equiv.), [1,1'-bis(diphenylphosphino)ferrocene]palladium(II) (6.04 mg, 0.00825 mmol, 0.058 equiv.), and zinc (14.0 mg, 0.214 mmol, 1.5 equiv.) were dissolved in 4.5 mL of THF. The solution was reacted under a nitrogen atmosphere at 70° C for 24 h. After dichloromethane was added, the organic phase was washed with H_2O 3 times, dried over Na_2SO_4, and then filtered to give a crude material. The crude material was purified by column chromatography (silica gel; eluent = 10 % dichloromethane/hexane) to give **3d** (43.2 mg, 67%) as a white powder. The deuteration yield of **3d** was determined by

comparing peak areas in 1H NMR spectra of an **3h** with those in the 1H NMR spectra of a **3d** sample. Dibromomethane (10 mg) in chloroform-*d* (10 mL) was used as the solvent for NMR measurements (Fig. S4a and S4b). The peak area of CH_2Br_2 was normalized in each spectrum. The deuteration yield of the DBC backbone was calculated to be 85%. MALDI TOF (m/Z): [M]+ calculated for $C_{32}H_5D_{15}S$, 451.2227; Found, 451.219 (Fig. S4c).

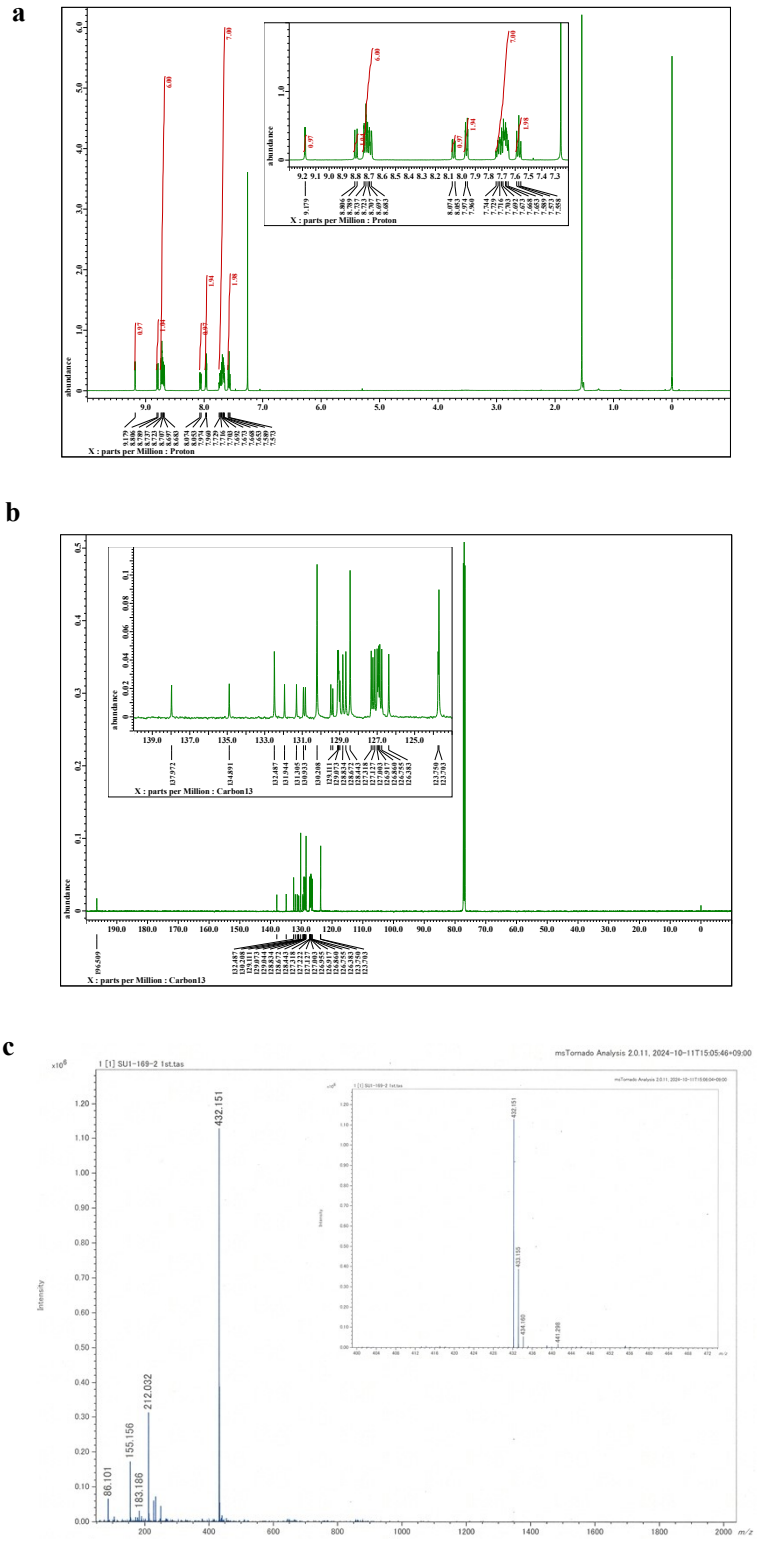

Fig. S1. ^{1}H NMR (a), ^{13}C NMR (b), and HRMS-MALDI (c) spectra of **2h**.

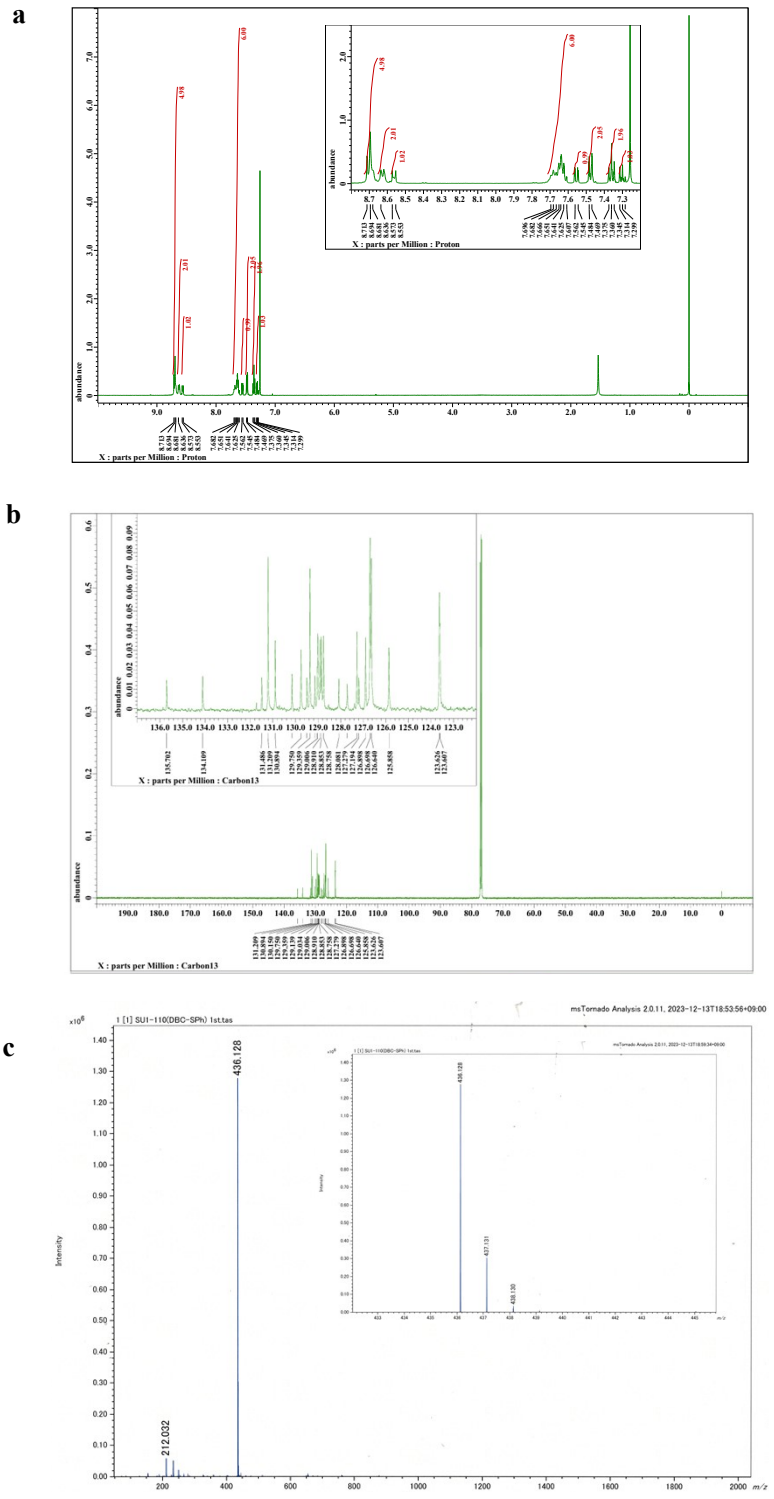

Fig. S2. ^{1}H NMR (a), ^{13}C NMR (b), and HRMS-MALDI (c) spectra of **3h**.

a

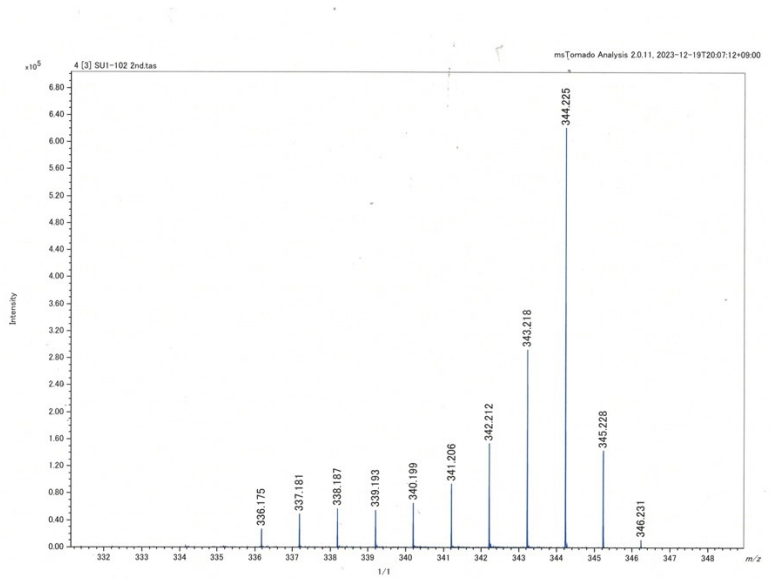
msTornado Analysis 2.0.11, 2023-12-19T20:07:12+09:00
4 [3] SU1-102 2nd.tas
x10^5
Intensity
m/z
1/1
336.175
337.181
338.187
339.193
340.199
341.206
342.212
343.218
344.225
345.228
346.231

b

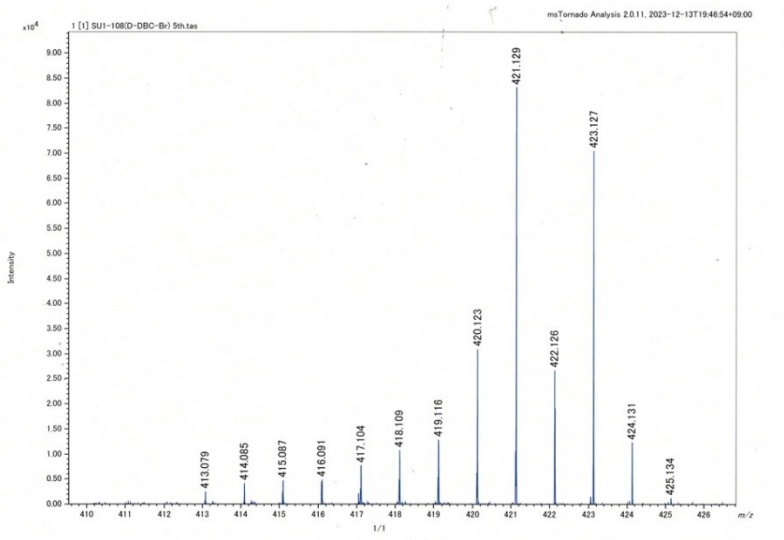

Fig. S3. MALDI TOF spectra of dibenzo[*g,p*]chrysene-d_{16} (a) and 2-bromodibenzo[*g,p*]chrysene-1,3,4,5,6,7,8,9,10,11,12,13,14,15,16-d_{15} (b).

a

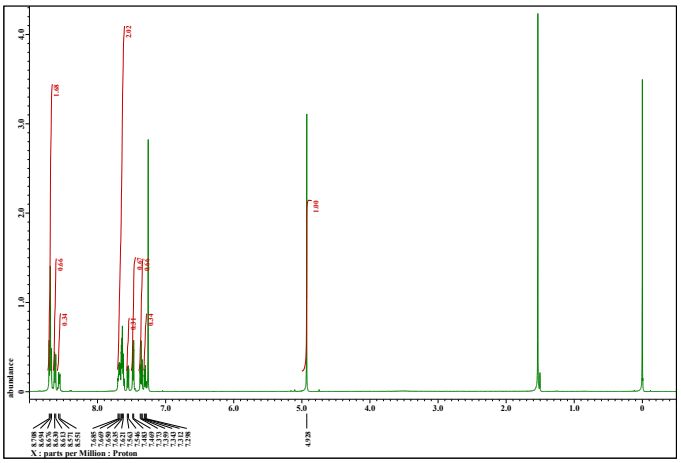

b

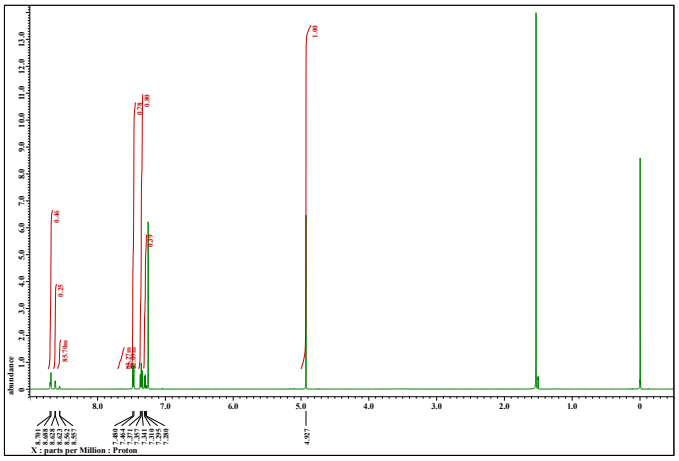

c

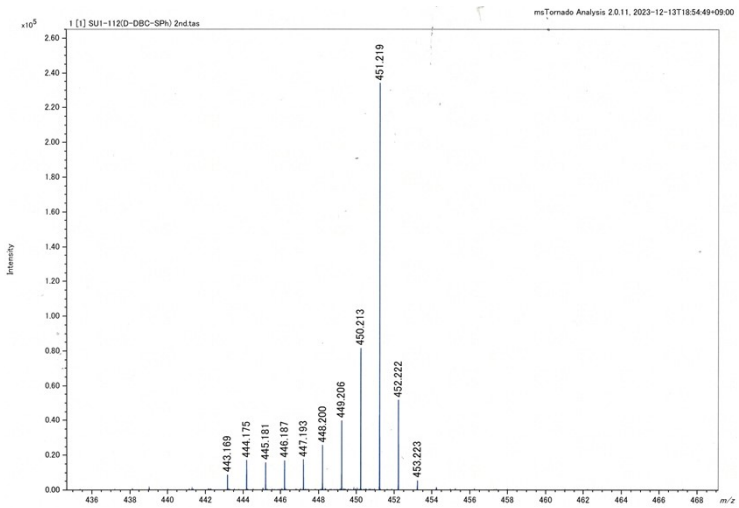

Fig. S4. ^{1}H NMR spectrum of **3h** (a), ^{1}H NMR spectrum of **3d** (a), and HRMS-MALDI spectrum of **3d**.

2. Preparation of films doped with guest chromophores

0.3 mg of guest molecule powder and 99.7 mg of benzophenone powder were mixed and heated to 80°C, which is above the melting point of benzophenone. After melting of benzophenone, the guest was dissolved into the melted benzophenone. The melted solution was sandwiched between two quartz substrates on a hot plate at 80°C. Then it was cooled to RT. The solution was then touched with a spoon to induce crystallization of benzophenone, and a host-guest film in which the guest was doped into the benzophenone polycrystalline host was obtained between the two quartz substrates.

3. Photophysical measurement and determination of Φ_p (Figure S5-S7, and Table S1)

The absorption spectra of the solutions and thin films were measured using a absorption spectrometer (V-760, JASCO, Japan). The excitation unit of a spectrophotometer (FP-8300, JASCO, Japan) was used to provide excitation light for measuring the emission spectra of solutions and films. The emission spectrum and intensity during and after excitation light irradiation were measured using a photonic multichannel analyzer (C10027-01, Hamamatsu Photonics, Japan).

The luminescence quantum yield under 310 nm-excitation light (Φ_e) in 570-849 nm for film pyrene, 534-809 nm for film 1h, 520-867 nm for film 2h, 534-868 nm for film 3h, and film 3d was measured in air using an absolute quantum yield measurement system (G9920-02G, Hamamatsu Photonics, Japan) (blue line, Fig. S5). Φ_e for films pyrene, 1h, 2h, 3h, and 3d were determined to be 2.4, 7.6, 10.7, 12.4, and 28.8%, respectively. By comparing the relative intensities of the emission spectra under excitation light and 20-40 ms after the excitation light irradiation was stopped are shown in Fig. S6. Φ_p was determined from the area ratio of the red line (S_e) to the green line (S_p) in 570-849 nm for film pyrene, 534-809 nm for film 1h, 520-867 nm for film 2h, 534-868 nm for film 3h, and film 3d based on the following formula: $\Phi_p = \Phi_e S_p/S_e$ (Fig. S7) Φ_p of films pyrene, 1h, 2h, 3h, and 3d were determined to be 1.5, 7.6, 8.8, 12.4, and 28.8%, respectively. In Fig. S5 and S6, a weak excitation intensity to allow linear increase of RTP vs excitation intensity was used because a strong excitation intensity causes the decrease triplet annihilation to decrease RTP yield. This direction has been used for 12 years and the validity of this method is explained in detail in a review article[S2,S3].

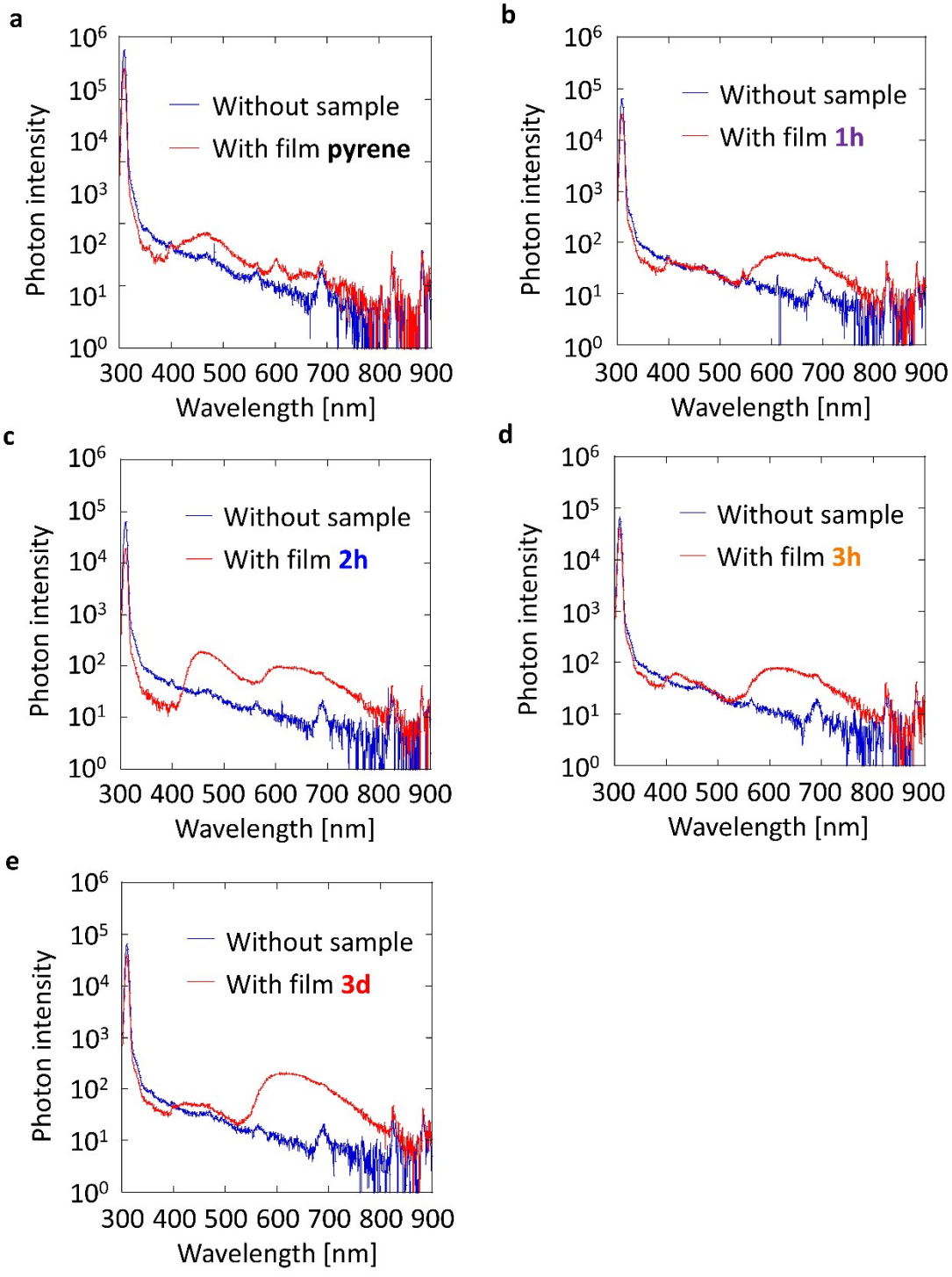

Fig. S5. Photon intensity spectral profile in the absence (blue) and presence (red) in an integration sphere under 310 nm-excitation for films pyrene (a), 1h (b), 2h (c), 3h (d) and 3d (e).

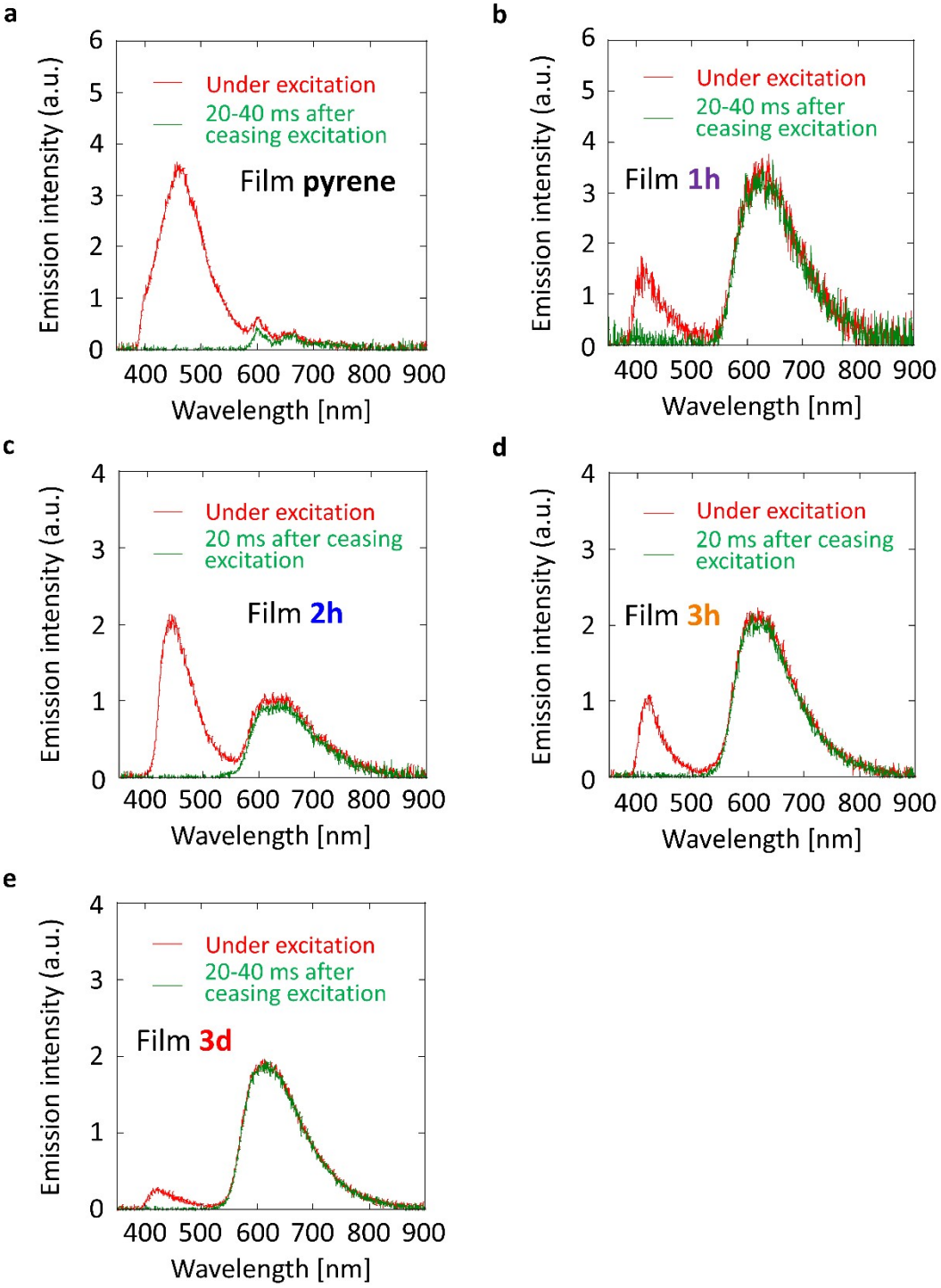

Fig. S6. Emission spectral intensity under and soon after (20-40 ms) ceasing excitation at 310 nm for films pyrene (a), 1h (b), 2h (c), 3h (d) and 3d (e).

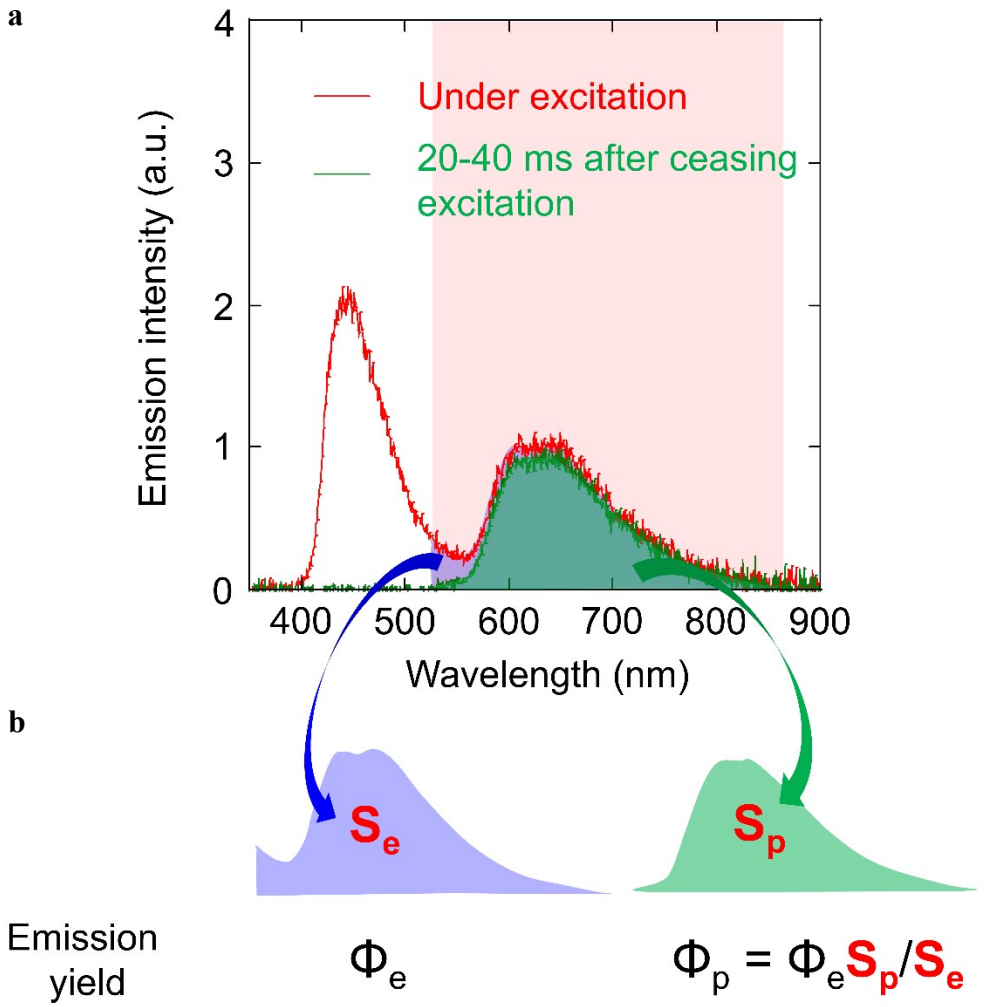

Fig. S7. A method for separating fast emission from persistent room-temperature phosphorescence for the determination of phosphorescence quantum yield using the example from film 2h. (a) Emission intensity of a film for 20 ms exposure time under excitation (red) and emission intensity of a film for 20 ms exposure time in the time range of 20-40 ms after ceasing the excitation (green). (b) Illustration explaining how to determine Φ_p from the area ratio of emission.

Table S1. Summary of phosphorescence quantum yields and average phosphorescence lifetimes for materials that exhibit the average emission lifetime > 100 ms and the single afterglow emission peak > 600 nm.[S4-S10].

λ_p (nm)	Φ_p (%)	τ_p (s)	Reference
623	8.3	0.13	B. Chen *et al.*, *Angew. Chem. Int. Ed.*, 2021, **60**, 16970-16973.[S4]
600	9.2	0.33	X. Fuming *et al*., *Nat. Commun*., 2022, **13**, 186.[S5]
623	8.0	0.22	X. Fuming *et al*., *Nat. Commun*., 2022, **13**, 186.[S5]
643	6.3	0.20	X. Fuming *et al*., *Nat. Commun.*, 2022, **13**, 186.[S5]
657	5.4	0.18	X. Fuming *et al.*, *Nat. Commun*., 2022, **13**, 186.[S5]
681	4.2	0.11	X. Fuming *et al*., *Nat. Commun.*, 2022, **13**, 186.[S5]
626	2.9	0.58	K. Fukasawa *et al*., *J. Phys. Chem. Lett.*, 2022, **13**, 7788.[S1]
631	3.9	0.49	K. Fukasawa *et al*., *J. Phys. Chem. Lett.*, 2022, **13**, 7788.[S1]
626	6.6	0.61	K. Fukasawa *et al*., *J. Phys. Chem. Lett.*, 2022, **13**, 7788.[S1]
624	16	1.8	K. Fukasawa *et al*., *J. Phys. Chem. Lett.*, 2022, **13**, 7788.[S1]
610	13.1	0.34	D. Li *et al.*, *Sci. Adv.*, 2022, **8**, eabl8392.[S6]
614	3.2	0.59	J. Jovaišaitė *et al*., *Angew. Chem. Int. Ed.*, 2023, **62**, e202215071.[S7]
608	12	0.5	X. Shen *et al*., *Chem. Commun.*, 2023, **59**, 7036-7039.[S8]
625	11.87	4.0	X. Zheng *et al.*, *Mater. Horiz*. 2023, **10**, 197-208.[S9]
625	8.7	0.64	S. Bahadur *et al.*, *Adv. Sci.*, 2024, **11**, 2308897.[S10]
625	21	1.6	S. Bahadur *et al.*, *Adv. Sci.*, 2024, **11**, 2308897.[S10]
612	12.4	0.48	This paper
611	28.8	1.47	This paper
649	8.6	0.35	This paper
628	7.6	0.49	This paper

Pure RTP with a lifetime of 100 ms or more shows almost no light decay below 100 ms. On the other hand, afterglow emission due to delayed fluorescence has a large light decay in the millisecond region after the light is turned off. Therefore, the average emission lifetime is much shorter. Whether or not such decay occurs can be shown by separating the light yield in each time region as in the example in Ref. S11 or Fig. S9. In this table, data without a large initial decay in the millisecond region has been selected.

4. Demonstration of red persistent phosphorescence under room light (Figure S8)

Films pyrene, 1h, 2h, 3h, and 3d with absorbances ranging from 0.5 to 1 in the wavelength range at 350 nm were prepared (Fig. S8a). Images of the films under ultra-violet (UV) light and after 20-40 ms of UV light exposure were captured by a camera (i-phone SE-3, Apple. Inc, USA) under room light. A handy UV lamp (SLUV-6, AS ONE, Japan) was used for UV light. UV light intensity at the sample position and room light intensity were measured using power meter (S130VC, Thorlabs, USA). The intensity of the room light (Fig. S8b) where the sample was placed was 0.12 mW/cm^2 when all the photons of the room light are converted to 532 nm. This is equivalent to 3.2×10^{14} photons being irradiated to 1 cm^2 per 1 s. Roughly approximating that 10% is reflected off the quartz surface, approximately 3.2×10^{13} photons/cm^2 of white light reaches the camera per 1 s (Fig. S8d and S8e, (iv)). The intensity of the UV light at the location where the sample was placed (Fig. S8b) was 0.22 (mW/cm^2) in terms of a wavelength of 360 nm. This is calculated as 4.0×10^{14} photons irradiated to 1 cm^2 per 1 s.

When the excitation light was applied to films pyrene and 3h, the film pyrene emitted weak blue fluorescence while no red light was observed when the UV light was turned off (Fig. 1d, Fig. S8c). On the other hand, in films 3h and 3d, clear red emission was observed even under room light immediately after UV light irradiation was stopped (Fig. 1d, Fig. S8c). This behavior is also logically ensured by the following considerations.

In the films, half of the 3.2×10^{14} (photons/cm^2) in UV light are approximately absorbed by the sample under the excitation light per 1 s (Fig. S8d and S8e; (i)) when absorbance in 300-400 nm are considered. Therefore, 1.6×10^{14} singlet excitons are formed within a range of 1 cm^2 per 1 s (Fig. S8d and S8e; (ii)). Since the yield of

phosphorescence after singlet exciton formation is Φ_p, taking into account the quantum yields of samples pyrene, 1h, 2h, 3h, and 3d, the following phosphorescence photons are emitted from the samples per unit time:

Film pyrene：$2.8\times10^{14} \times 0.015 = 4.2\times10^{12}$ photons/cm^2

Film 1h：$2.8\times10^{14} \times 0.076 = 2.1\times10^{13}$ photons/cm^2

Film 2h：$2.8\times10^{14} \times 0.084 = 2.4\times10^{13}$ photons/cm^2

Film 3h：$2.8\times10^{14} \times 0.124 = 3.5\times10^{13}$ photons/cm^2

Film 3d：$2.8\times10^{14} \times 0.288 = 8.1\times10^{13}$ photons/cm^2

For example, the number of photons of red phosphorescence emitted by film pyrene at 4.2×10^{12} photons/cm^2 s (Fig. S8d; (iii)) is much smaller than the number of photons (3.2×10^{13} photons/cm^2 s) in the reflection of ambient white light intensity (Fig. S8d, (v)). Therefore, red light cannot be perceived under white light. On the other hand, in film 3h, the number of red phosphorescent photons emitted from film 3h (3.5×10^{13} photons/cm^2 s, Fig. S8e, (iii)) is at the same level as the number of photons (3.2×10^{13} photons/cm^2 s) in the reflection of the intensity of the surrounding white light (Fig. S8e, (v)). Therefore, sufficient red persistent RTP can be well distinguished even under white light. Therefore, the present measurement of Φ_p logically explains the behavior of the afterglow intensity observed both in real life and in camera measurements.

In film pyrene, red phosphorescence with Φ_p = 9.2% and an average phosphorescence lifetime (τ_p) of 0.33 s has been reported. Our group has been able to reproduce τ_p, but only a tenth of the reported value for Φ_p. Even when using various concentrations of pyrene added to benzophenone or high purity benzophenone reagent, Φ_p could not exceed 2% currently.

In addition, in samples with $\Phi_p \simeq 10\%$, the red intensity becomes sufficiently

noticeable when irradiated with excitation light because blue fluorescence quantum yield is not high when benzophenone crystals are used as host. However, in the reported photographs, the blue intensity is dominant under excitation light. Therefore, this point is a questionable point that is significantly different from the behavior of our films that show a red persistent RTP of 10% or more.

Different estimates of Φ_p by a factor of 10 or more could, for example, cause a 10% yield to be mistaken for nearly 100%. Since verification of the demonstration examples in this paper may also contribute to various researchers obtaining the comparable data for the same sample, it will be useful to summarize the points that can be easily checked as follows.

(1) The quantum yield of luminescence under excitation light irradiation was plotted together with the raw data (Fig. S5).

(2) The emission spectrum intensities during excitation light irradiation and 20 ms -100 ms after the irradiation was stopped should be shown without normalization so that the spectral intensities can be compared (Fig. S6).

These two allow scientists to correctly know the value of Φ_p from the data.

Some groups may not have an integrating sphere or a CCD spectrometer. However, even in that case, you can check the approximate degree of Φ_p with just a smartphone camera and a handheld UV light using the following (3)-(6) processes.

(3) DBC (**1h**) and benzophenone are commercially available. A crystalline film doped with benzophenone at a concentration of 0.3 wt% DBC (reference film) shows red phosphorescence with Φ_p = 5-10% and a lifetime of about 0.5 s. Place this reference film next to your sample film that shows persistent RTP at long wavelengths.

(4) In step (3), keep the camera exposure time and other settings fixed and ensure that the

camera intensity does not saturate.

(5) In the case of the two thin films in step (3), make sure that their absorbance at the excitation wavelength is equivalent.

(6) Measure the time-dependent change in luminescence intensity of the two films under and after UV irradiation (approximately 0.1-0.2 mW/cm^2) with a camera on the same screen.

In this process (6), the degree of Φ_p of the sample film can be confirmed by comparing the emission intensity between the sample film and the reference film for 20 ms to 100 ms after the excitation light irradiation is stopped.

In recent years, the correlation between experimental and calculated values regarding k_p and k_{nr} has become better when vibrations and distortion of chemical structures are considered. On the other hand, if the data of optically observed Φ_p is not reliable, the correlation properties are difficult to obtain. Therefore, proposals such as those in this section are becoming important to the scientific community.

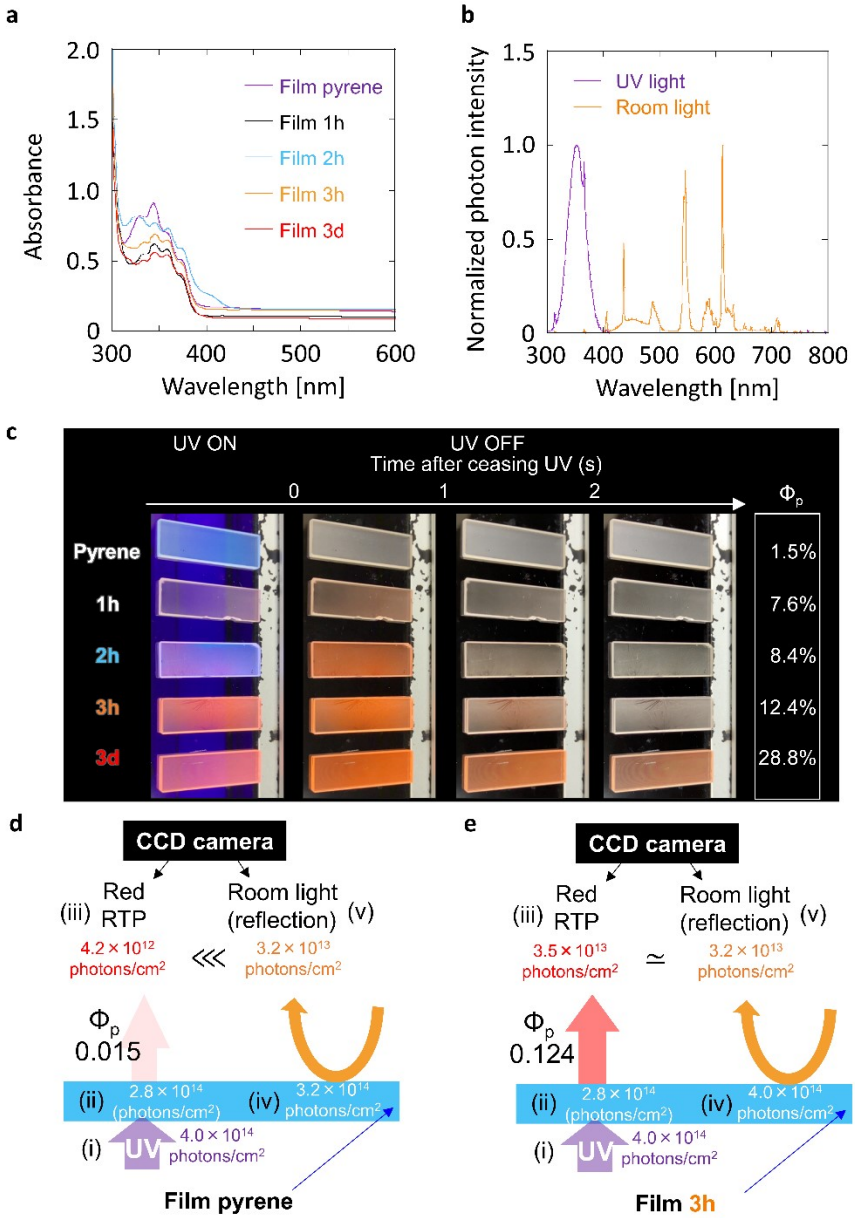

Fig. S8. Detailed explanation of demonstration in Fig. 1c. (a) Absorption spectra of films pyrene, 1h, 2h, 3h, and 3d. (b) Spectra of UV light and room light from fluorescence tube used in the demonstration. (c) Emission behavior from films pyrene, 1h, 2h, 3h, and 3d under and soon (20-50 ms) after ceasing the UV excitation under the room light condition. (d) Approximate estimation of the relationship among photon intensity of UV light, red RTP from film pyrene, and reflection from room light. (e) Approximate estimation of the relationship among photon intensity of UV light, red RTP from film 1h, and reflection from room light.

5. Phosphorescence decay characteristics from 1 ms to 10 s (Figure S9)

The phosphorescence decays of the films after these 310-nm excitations are shown in Fig. S9. The luminescence decay from 2 ms to 200 ms was measured using a spectrophotometer (FP-8300, JASCO, Japan). The luminescence decay from 20 ms to 10 s was determined using the equipment and methods described in Section S3. Using these two pieces of information, Fig. S9 was constructed. In the log-log plot of emission intensity vs. time, emission hardly decreases by 100 ms, which is suitable for measuring the stronger intensity with a two-dimensional optical detector between 0.1 and 1 s.

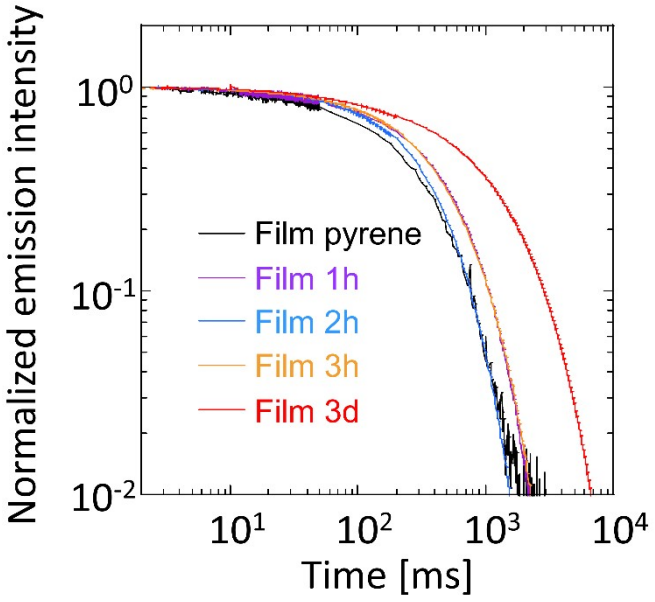

Fig. S9. RTP decay characteristics in 2 ms -10 s of films pyrene, 1h, 2h, 3h, and 3d.

6. Measurement procedure of Φ_t in solution (Figure S10, Table S2 and Table S3)

The yield of triplet from the lowest singlet excited state (S_1) of **3h** was confirmed by a method using triplet-triplet energy transfer from the pigment to *β*-carotene[S12,S13]. The following sample and reference solutions were used in this method. The sample solution contained one of the synthesized chromophores (**3h**) as a triplet sensitizer and *β*-carotene (1.0×10^{-3} M) as an acceptor in benzene. In the reference solution, benzophenone was used as a triplet sensitizer and *β*-carotene (1.0×10^{-3} M) was used as an acceptor in benzene. In this solution, the concentration of the triplet photosensitizing dye was adjusted so that the Abs at 355 nm was 1 when the solution was placed in a quartz cell with a thickness of 1 mm. The solutions were degassed using the freeze–dry pump method three times and sealed immediately before the measurements.

The time change of transient absorption at 530 nm of the sample and reference solutions were measured using a sub-nanosecond transient absorption spectrophotometer (picoTAS, Unisoku, Osaka, Japan) with a 355-nm Q–switched microchip laser (PNV–M02510–1×0, Teem Photonics, Meylan, France) to obtain data in Fig. S10a. For the sample and reference solutions, values of A, B, τ_1 and τ_2 were determined from the fitting data of Fig. S10a using $A(1–\exp(–t/\tau_1))\exp(–t/\tau_2) + B\exp(–t/\tau_1)$ equation, where t is the time after irradiation of an excitation pulse at 355 nm. Values of A, B, τ_1 and τ_2 are summarized in Table S2. We note the optics and excitation power at 355 nm were unchanged between the sample and the reference solution. Next, the time course of transient absorption of the sample solution in the absence of *β*-carotene and the reference solution in the absence of *β*-carotene was also measured (Fig. S10b). From these decays, the triplet lifetime (τ_0) of **3h** and benzophenone in benzene was determined as shown in Table S3.

The efficiency of the energy transfer from the lowest triplet excited state (T_1) of the triplet sensitizer to T_1 of β-carotene (Φ_{TT}) in the benzene solution was calculated by using $\Phi_{TT} = (\tau_0 - \tau_1)/\tau_0$.

$$A_s/A_r = \Phi_{ts}\Phi_{TTs}/\Phi_{tr}\Phi_{TTr}, \qquad (1)$$

where A_s and A_r are A of sample and reference solutions, respectively, Φ_{ts} and Φ_{tr} are Φ_t of sample and reference solutions, respectively, Φ_{TTs} and Φ_{TTr} are Φ_{TT} of sample and reference solutions, respectively. Φ_{ts} and Φ_{tr} correspond to the intersystem crossing yield (Φ_{isc}) from the lowest singlet excited state to triplet states of sensitizers in benzene solution. Because Φ_{tr} of benzophenone as a triplet sensitizer in the reference solution tends to be 1, Φ_{ts} of **3h** as a triplet sensitizer in the sample solution is determined to 0.81 using equation (1). In other words, Φ_{isc} for **3h** is determined to be 0.81.

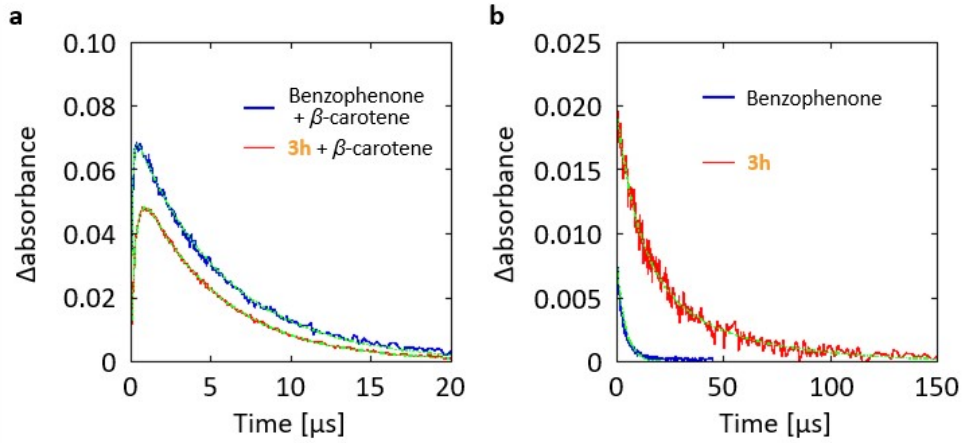

Fig. S10. (a) Transient absorption intensity changes at 530 nm of sample and reference solutions. The sample solution is benzene solution in which **3h**, a triplet sensitizer, and β-carotene as an acceptor are dissolved. The reference solution is benzene solution in which benzophenone as a triplet sensitizer and β-carotene as an acceptor are dissolved together. (b) Transient absorption intensity changes at 530 nm of sample and reference solutions in the absence of β-carotene. In (a) and (b), the solutions are degassed using the freeze-dry pump method 3 times and sealed just before measurements. Absorbance at 355 nm caused by the triplet sensitizer of the solutions is set to 1.0 in a quartz cell with thickness of 1 mm. The green lines in (a) and (b) are fitting curves based on the data in Table S2 and S3, respectively.

Table S2. Summary of physical properties used in Fig. S10a. This is used to determine Φ_t for **3h**.

Role of the solution	Triplet sensitizer	Concentration of β-carotene (M)	A	B	τ_1 (μs)	τ_2 (μs)	Φ_{TT}	Φ_{isc}
Sample	3h	1.0×10^{-3}	0.0610	0.00541	0.319	5.06	0.991	0.81 (±20)
Reference	Benzophenone		0.0741	0.0158	0.103	5.69	0.974	1.0

Table S3. Summary of physical properties used in Fig. S10b. This is used to determine Φ_t for **3h**. τ_0 is determined based on $\tau_0 = (C_1\tau_{C1}^2 + C_2\tau_{C2}^2)/(C_1\tau_{C1} + C_2\tau_{C2})$.

Compounds	C_1	C_2	τ_{C1} (μs)	τ_{C2} (μs)	τ_0 (μs)
3h	0.00766	0.0118	42.7	10.5	33.9
Benzophenone	0.000876	0.00779	0.00250	3.95	3.95

7. Photophysical characteristics in amorphous *β*-estradiol (Figure S11)

0.3 mg of guest and 99.7 mg of *β*-estradiol powder were mixed. The powder was heated to 240°C, and the guest was dissolved in the molten *β*-estradiol in a short time. The solution was sandwiched between two quartz substrates at 240°C, and then rapidly cooled to RT to obtain a film in which an amorphous film of host-guest was sandwiched between two quartz substrates[S2]. In this paper, the amorphous *β*-estradiol film using 1h and 3h as a guest is defined as films S1h and S3h, respectively. The Φ_p and phosphorescence lifetime of the films S1h and S3h were measured using the same method as in Section S3. Details of the optical properties are shown in Fig. S11.

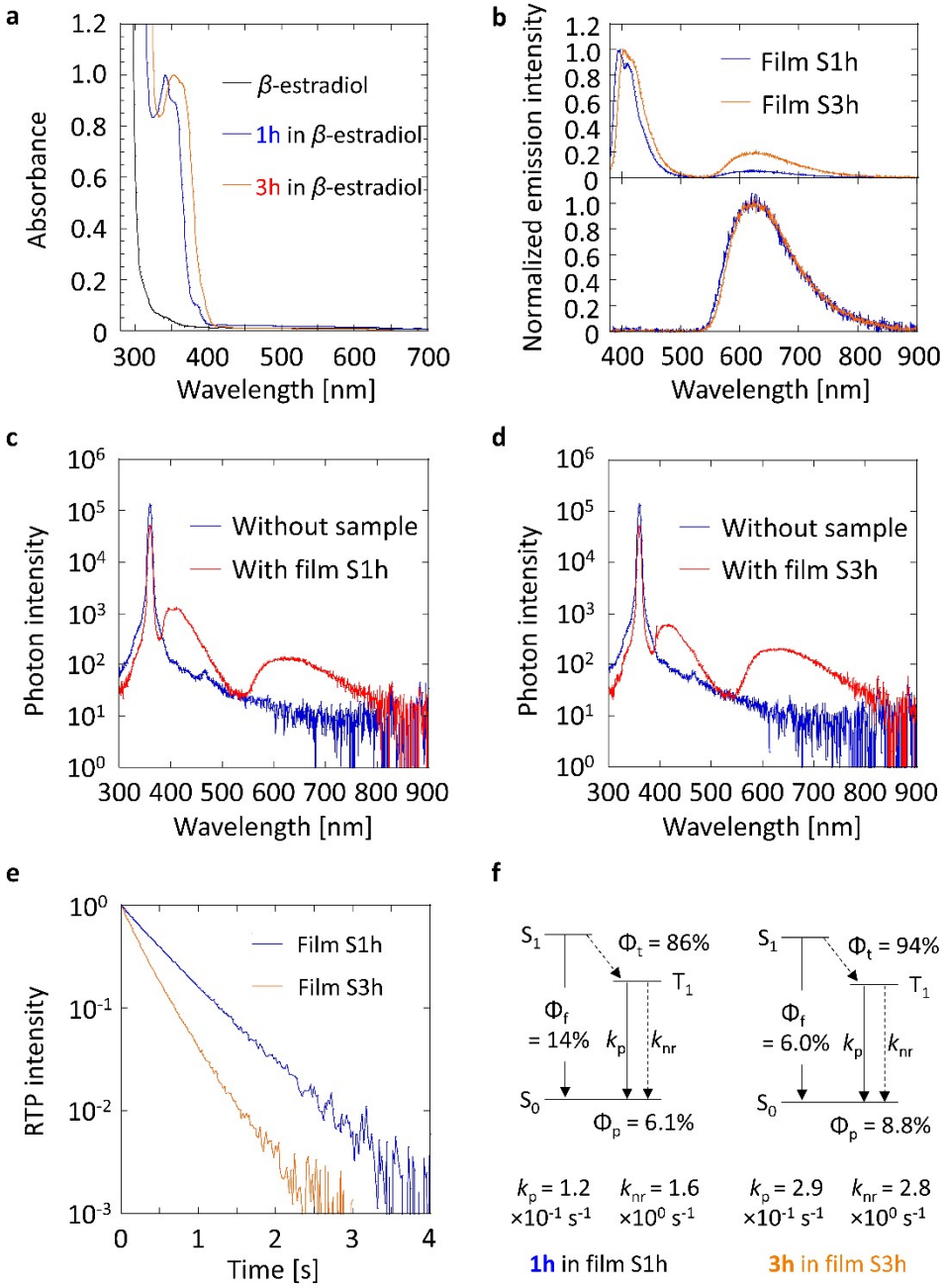

Fig. S11. Optical properties of films S1h and S3h. (a) Absorption spectra. (b) Emission spectra under and soon (20 ms-40 ms) after easing excitation at 360 nm. (c,d) Photon intensity spectral profile in the absence (blue) and presence (red) in an integration sphere under 360 nm-excitation for films S1h (c) and S3h (d). (e) RTP decay characteristics. (f) Description of excited state dynamics when light at 360 nm is irradiated to the films S1h (left) and S3h (right).

8. Comparison of triplet generation quantity of guests in films (Figure S12-S14)

To confirm the difference in Φ_t between films 1h and 3h, the molar absorption coefficient (ε_{TT}) of **1h** and **3h** was determined by the following method. Three types of benzene solutions were prepared by dissolving benzophenone, **1h**, and **3h**, respectively. The triplet-triplet (T-T) absorption decays of these solutions with absorbance values of 1 at a wavelength of 355 nm in a 1 mm thick quartz cell are shown in Fig. S12. ε_{TT} of benzophenone in benzene at 532 nm is 7.2×10^3 M^{-1} cm^{-1} [S14]. Therefore, by comparing the heights in Fig. S12, ε_{TT} of **1h** at 530 nm was determined to be 3.3×10^3 M^{-1} cm^{-1}, and ε_{TT} of **3h** at 530 nm was determined to be 7.4×10^3 M^{-1} cm^{-1}. Thus, the TT absorption spectra of **1h** and **3h** were determined as shown in Fig. S13a. The comparable shape of TT absorption spectra were also observed in quantum chemical calculations (Fig. S13b).

Next, comparable Φ_t between films **1h** and **3h** was confirmed by the following method[S15,S16]. The absorption at 360 nm of films 1h and 3h is equivalent. The Δabsorbance at 460 nm was measured for these two films when irradiated with an excitation light intensity of 360 nm (Fig. S14). For both films, the Δabsorbance at 460 nm increased with increasing excitation light intensity at 360 nm. The slope of Δabsorbance and excitation light intensity in the weak excitation region is logically proportional to Φ_t and ε_{TT} at 460 nm. Since the ε_{TT} at 460 nm for **1h** and **3h** are equivalent (Fig. S13a), the Φ_t for films 1h and 3h are equivalent. It is therefore confirmed that the difference in Φ_p between films 1h and 3h is caused by the difference in k_p and k_{nr}, not the difference in Φ_t. The saturation in the high concentration region is due to excitation annihilation and ground state breaching.

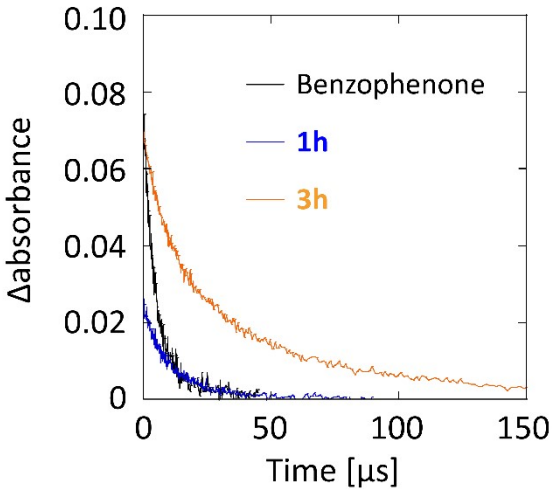

Fig. S12. Transient absorption decay characteristics of benzophenone, **1h**, and **3h** in benzene. The solutions are degassed using the freeze-dry pump method 3 times and sealed just before measurements. Absorbance at 355 nm caused by the triplet sensitizer of the solutions is set to 1.0 in a quartz cell with thickness of 1 mm.

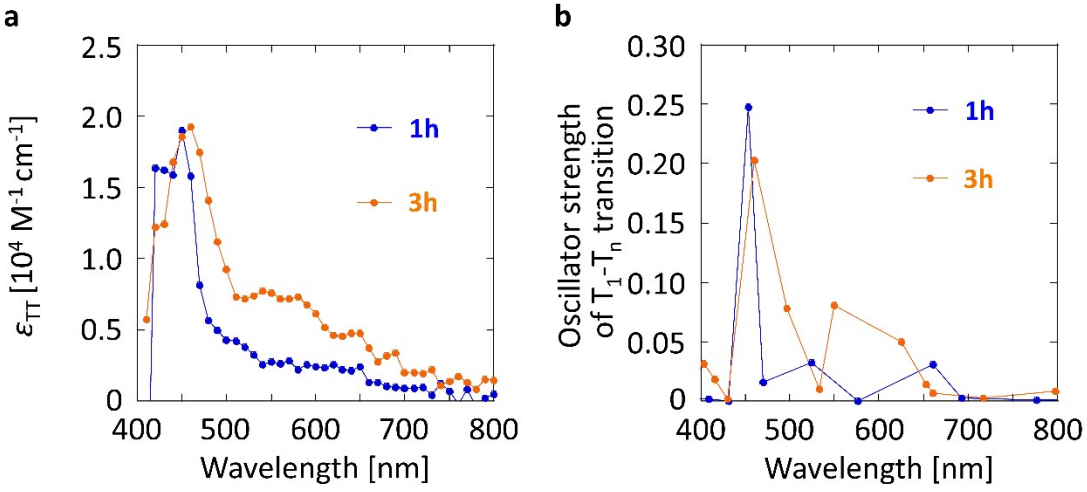

Fig. S13. (a) Spectra of ε_{TT} of **1h** and **3h** in benzene. (b) Oscillator strength spectrum of TT absorption of **1h** and **3h** calculated by quantum chemical calculation. The optimized structures at T_1 of **1h** and **3h** were determined by density functional theory (DFT) using Gaussian09 with B3LYP as the functional and 6-31G(d) as the basis set. The oscillator strength spectrum of TT absorption was calculated based on the optimized T_1 geometry by time-dependent DFT using Gaussian09 with B3LYP as the functional and 6-31G(d) as the basis set.

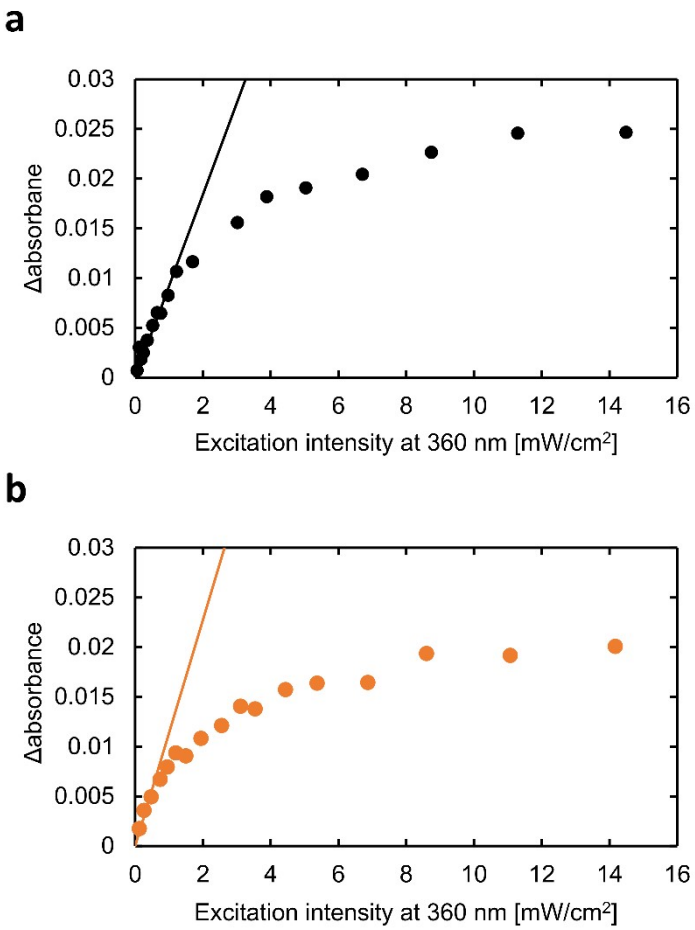

Fig. S14. Dependence of the transient absorption intensity of films 1h (a) and 3h (b) at a wavelength of 460 nm on the excitation light intensity. The films were irradiated with 360 nm light as the excitation light.

9. Temperature dependence of emission characteristics (Figure S15 and S16)

The temperature control of the temperature dependence of the luminescence properties of films 1h and 3h was performed by a cryostat (OptistatDN-V, Oxford Instrument, United Kingdom). The excitation light unit of a spectrophotometer (FP-8300, JASCO, Japan) was used for excitation of the samples. The luminescence properties from the samples were measured by a multi-channel analyzer (C10034-01, Hamamatsu Photonics, Japan). Φ_p at RT was determined using an integrating sphere as shown in Section 3. The phosphorescence intensity at 20-40 ms after ceasing excitation light intensity and the temperature dependence of the phosphorescence decay of films 1h and 3h are shown in Fig. S15a and S15b. Using the data on Φ_p at RT and the relative change in phosphorescence intensity at each temperature with respect to the phosphorescence intensity at RT, Φ_p at temperatures other than RT was determined. The change in phosphorescence intensity after the excitation light irradiation was stopped at each temperature was measured to determine the temperature dependence of τ_p (Fig. S15c and S15d). The temperature dependence of Φ_p and τ_p are summarized in Fig. S16a and S16b, respectively. By inserting k_p value into $\tau_p = 1/(k_p + k_{nr} + k_q)$ in each temperature, the temperature dependence of $k_{nr} + k_q$ was determined as Fig. S16c. The increase in $k_{nr} + k_q$ with increasing temperature in the low temperature range is due to k_{nr}[S2,S17,S18]. The Arrhenius plot of $k_{nr} + k_q$ was fitted with two exponential functions. From the fitted line of k_{nr}, the values of k_{nr} for **1h** and **3h** at RT were determined to be 1.7 s^{-1} and 1.8 s^{-1}, respectively.

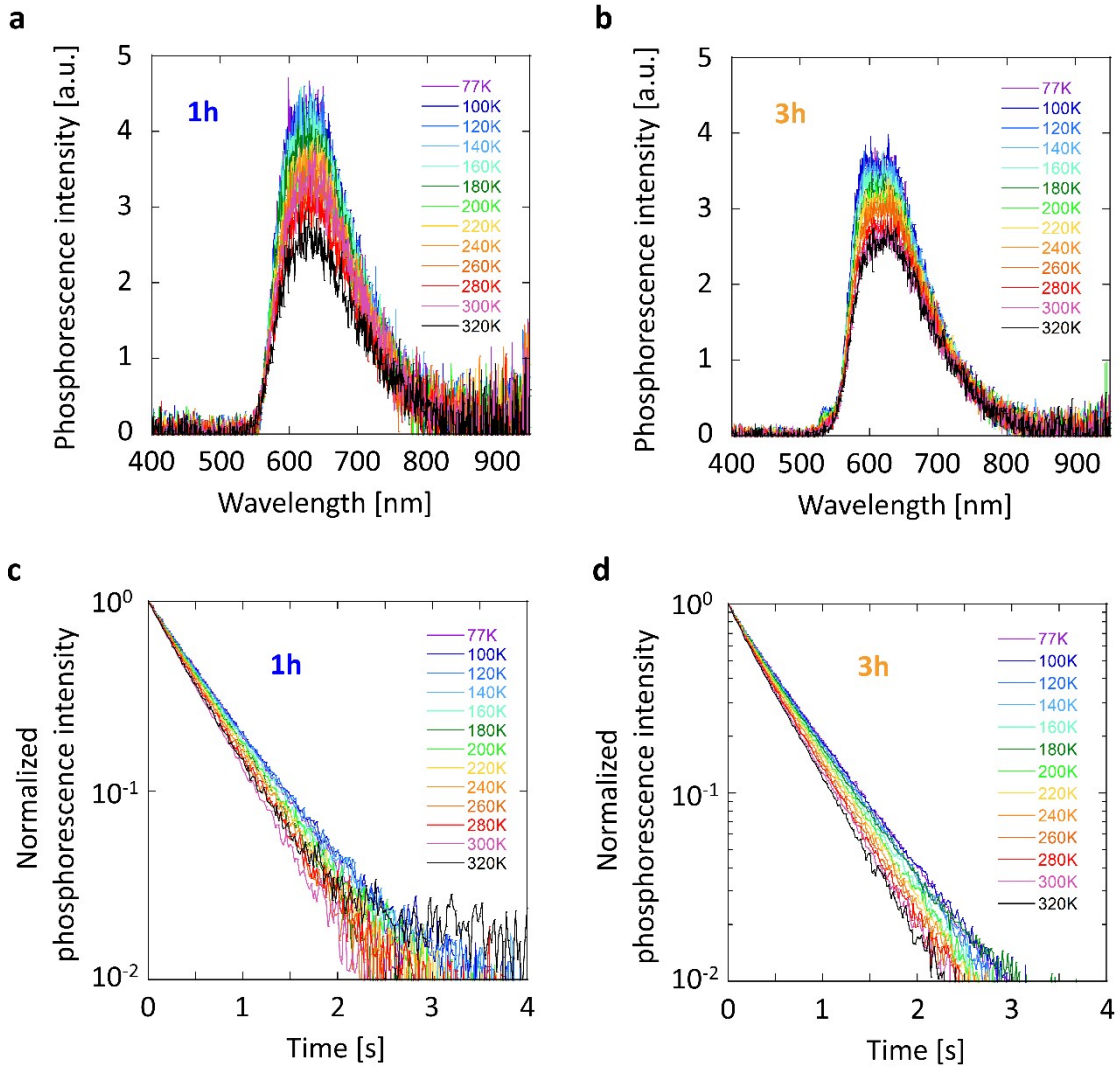

Fig. S15. (a,b) Temperature dependence of phosphorescence spectral intensity of films 1h (a) and 3h (b). (c,d) Temperature dependence of phosphorescence decay characteristics of films 1h (c) and 3h (d). Excitation wavelength is 310 nm.

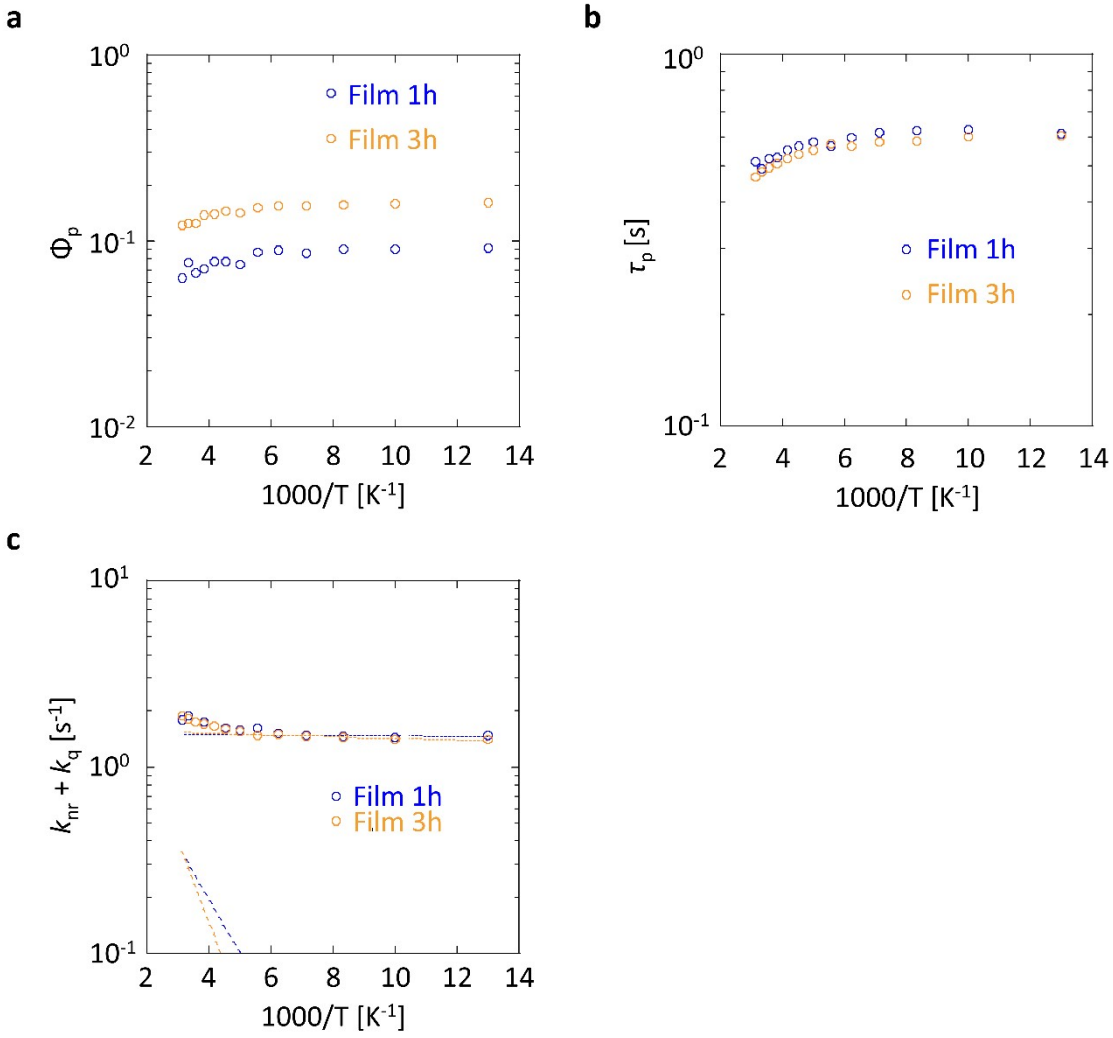

Fig. S16. Temperature dependence of Φ_p (a), τ_p(b), and $k_{nr} + k_q$ (c) of films 1h and 3h. Excitation wavelength is 310 nm. The dotted and dashed lines indicate the fitting lines of k_{nr} and k_q, respectively.

10. Summary of photophysical data of films (Table S4)

Table S4. Comparison of the physical factors related to the phosphorescence of thin films in this paper with previous reports. Since k_p cannot be determined without determining the triplet formation efficiency, the reference is limited to examples of red persistent RTP materials in which Φ_t is formed by actual measurement.

Guest*1	Host	Φ_t (%)	Φ_p (%)	τ_p (s)	k_p*4 (s^{-1})	$k_{nr} + k_q$*5 (s^{-1})	Reference
Pyrene	Crystalline benzophenone	95*2	1.5	0.34	0.046	2.9	This work
1h	Crystalline benzophenone	99*2 (87±22)*3	7.6	0.49	0.16	1.9	This work
2h	Crystalline benzophenone	92*2	8.8	0.35	0.27	2.6	This work
3h	Crystalline benzophenone	98*2 (81±20)*3	12.4	0.48	0.26	1.8	This work
3d	Crystalline benzophenone	98*2	28.8	1.47	0.20	0.48	This work
Dye S1	Amorphous *β*-estradiol	58*2 (61±15)*3	3.9	0.49	0.14	1.9	Reference S1
Dye S2	Amorphous *β*-estradiol	86*2 (99±25)*3	6.6	0.61	0.13	1.6	Reference S1
Dye S3	Amorphous *β*-estradiol	87*2 (99±25)*3	16.1	1.8	0.10	0.44	Reference S1
Dye S4	Amorphous *β*-estradiol	77*2 (85±21)*3	8.7	0.64	0.18	1.5	Reference S10
Dye S5	Amorphous *β*-estradiol	72*2 (88±22)*3	21.0	1.6	0.18	0.45	Reference S10

*1: Concentration is 0.3 wt%. *2: 1 - Φ_f, where Φ_f is the fluorescence yield. *3: Values of Φ_{isc} measured in benzene solution. *4: Value determined based on $k_p = \tau_p\Phi_p/\Phi_t$ using $\Phi_t = 1 - \Phi_f$. *5: Value determined based on $k_{nr} + k_q = 1/\tau_p - k_p$ using k_p in *3.

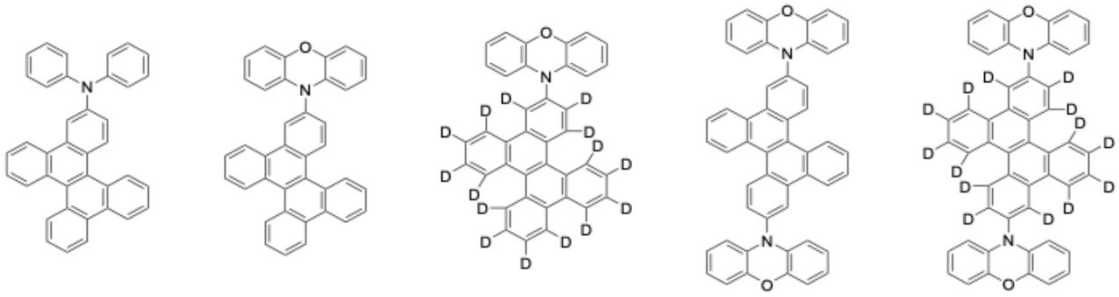

Dye S1 Dye S2 Dye S3 Dye S4 Dye S5

11. Quantum chemical calculation (Figure S17-S19)

The optimized structures at T_1 of **1h** and **3h** were determined by density functional theory (DFT) using Gaussian09 with B3LYP as the functional and 6-31G(d) as the basis set. In order to better reflect the state in benzophenone, the optimized structures at T_1 were determined under the dielectric constant (ε) of benzophenone. Concretely, the polarizable continuum model (PCM) of solvation was employed during T_1 geometry optimization, using benzophenone as the solvent with ε of 11.4 and universal force field radii. In the T_1 optimized structure, the T_1-S_0 transition energies of **1h** and **3h** were determined to be 1.58 eV and 1.57 eV, respectively (Fig. S17), and the equivalent phosphorescence energies were confirmed as in the experiment.

Single-point calculations to determine k_p and the spin-orbit coupling (SOC) between T_1 and S_0 ($\langle T_1|\boldsymbol{H}_{\mathbf{SO}}|S_0\rangle$) for each conformation determined by the method described below were performed using time-dependent DFT with the Amsterdam density functional (ADF) 2018 package. In the single point calculations to determine k_p, the transition dipole moment between the nth order singlet excited state (S_n) and S_0 (μ_{Sn-S0}), and the SOC between S_n and T_1 ($\langle S_n|\boldsymbol{H}_{\mathbf{SO}}|T_1\rangle$) were performed. The SOC operator within the zeroth-order regular approximation was $\hat{H}_{SO}$. The parameter $\langle S_n|\boldsymbol{H}_{\mathbf{SO}}|T_m\rangle$ was treated as a perturbation based on the scalar relativistic orbitals with the PBE0 functional and TZP basis sets. Scalar relativistic-time dependent DFT calculations included 10 singlet and 10 triplet excitations, which were used as the basis for the perturbative expansions in the calculations[S17-S19]. The conductor-like screening model (COSMO) of solvation, with benzophenone as the solvent (ε = 11.4 and radii = 3.0 Å), was used for the SOC calculations.

The k_p of **1h** was calculated using the optimized T_1 geometry determined above, as

described in the previous paragraphs.

The k_p of **3h** was calculated using the following method, taking into account the thermally activated conformation distribution. The conformational distribution due to heat treatment over **3h** was estimated as follows. In the optimized structures, the total energy at the T_1 state was calculated using DFT (Gaussian09/B3LYP/6-31G(d)) for structures in which θ_1 and θ_2 in Fig. 3a were arbitrarily changed by 10 degrees each. In this case, $\theta_1 = 0$ degrees and $\theta_2 = 90$ degrees were defined as the structure optimized for T_1. The T_1 energy difference (ΔE) for geometries with arbitrary θ_1 and θ_2 relative to the T_1-optimized geometry was calculated using DFT (Gaussian09/B3LYP/6-31G(d)) (Fig. S18a). Using $\Delta E(\theta_1, \theta_2)$ in the potential curve of T_1 (Fig. 3b), $p(\theta_1, \theta_2) = \exp(-\Delta E(\theta_1, \theta_2)/kT)/\Sigma\exp(-\Delta E(\theta_1, \theta_2)/kT)$ was calculated as the state distribution with respect to θ_1 and θ_2 for **3h** (Fig. S18b and Fig. 3c).A histogram of $k_p(\theta_1, \theta_2)$ for this distribution of θ_1 and θ_2 was calculated (Fig. S18c). Then the histogram of the product of $k_p(\theta_1, \theta_2)$ and $p(\theta_1, \theta_2)$ was confirmed (Fig. S18d and Fig. 3d). The integration of Fig. S18d (Fig. 3d), the average value of k_p was estimated to be 0.92 s^{-1}. The state in which ΔE was increased 8-fold in Fig. S19a was treated as a model in which **3h** was dispersed in a solid. The same analysis as in Figs. S18b, S18d, and S18f were performed for the solid model to show Fig. S19a, S19b, and S19c, respectively.

Theoretically, k_{nr} is proportional to the square of the SOC between T_1 and S_0 ($\langle T_1|\boldsymbol{H}_{SO}|S_0\rangle$). In the distribution of θ_1 and θ_2 in Fig. S19c, which correlates with the experimental values in the solid host, the central conformation is shown with θ_1 approaches 0° and θ_2 approaches 90°. In the **3h** conformation, the $\langle T_1|\boldsymbol{H}_{SO}|S_0\rangle^2$ between **3h** and **1h** hardly changes.

a

n	S_n energy [eV]	T_n energy [eV]
1	2.74	1.58
2	3.26	3.01
3	3.58	3.19
4	3.59	3.24
5	3.85	3.27
6	3.89	3.32
7	4.28	3.45
8	4.35	3.52
9	4.44	3.89
10	4.45	4.03

b

n	S_n energy [eV]	T_n energy [eV]
1	2.65	1.57
2	3.18	2.90
3	3.48	3.05
4	3.51	3.18
5	3.75	3.25
6	3.86	3.30
7	3.89	3.43
8	3.95	3.56
9	4.26	3.67
10	4.31	3.78

Fig. S17. Calculated energies of the excited singlet and triplet states of **1h** and **3h**.

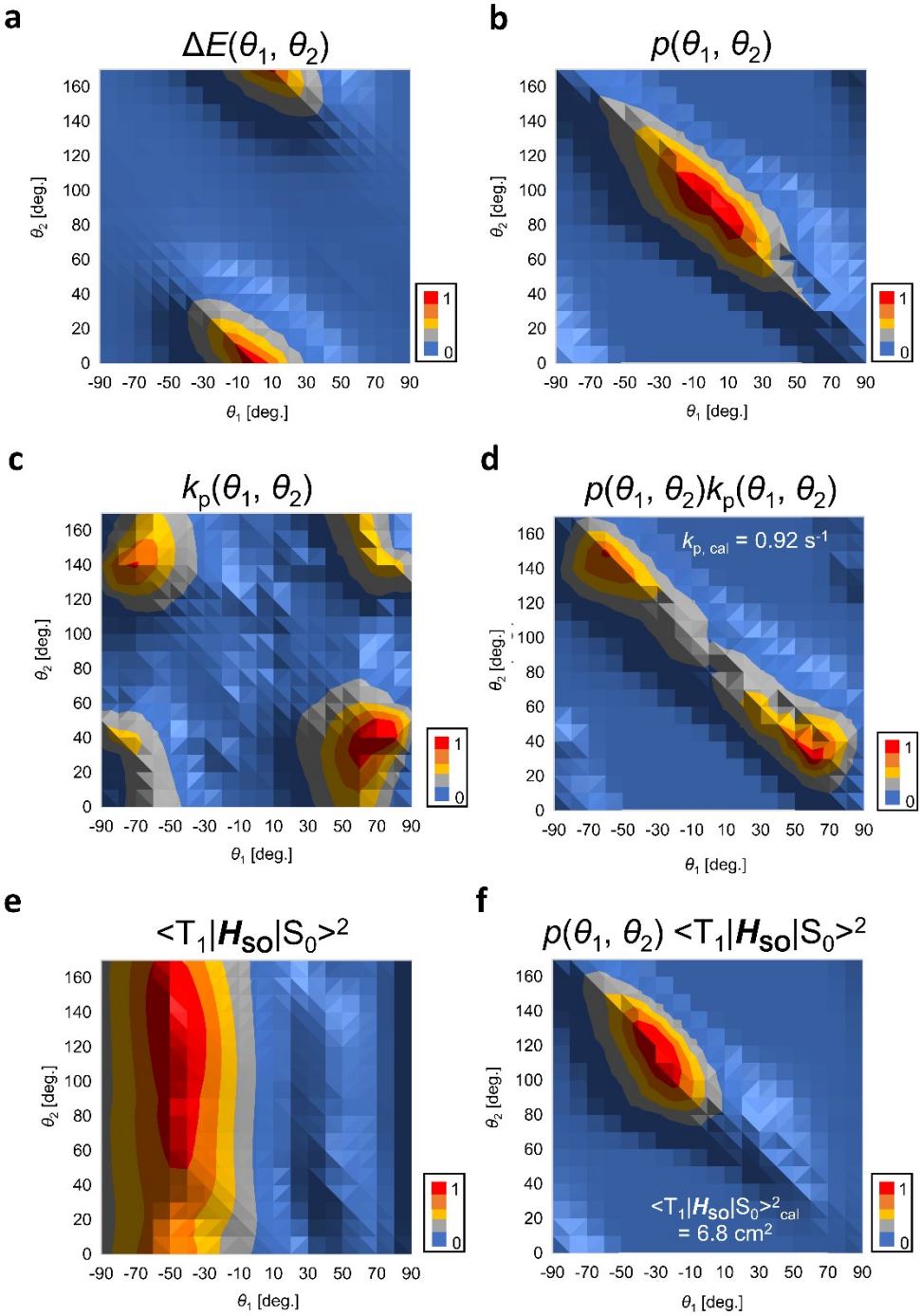

Fig. S18. Histogram of $\Delta E(\theta_1, \theta_2)$ (a), $p(\theta_1, \theta_2)$ (b), $k_p(\theta_1, \theta_2)$ (c), $k_p(\theta_1, \theta_2)p(\theta_1, \theta_2)$ (d), $\langle T_1|\boldsymbol{H}_{SO}|S_0\rangle^2$ (e), and $\langle T_1|\boldsymbol{H}_{SO}|S_0\rangle^2 p(\theta_1, \theta_2)$ (f) when **3h** is located in isolated condition in vacuum.

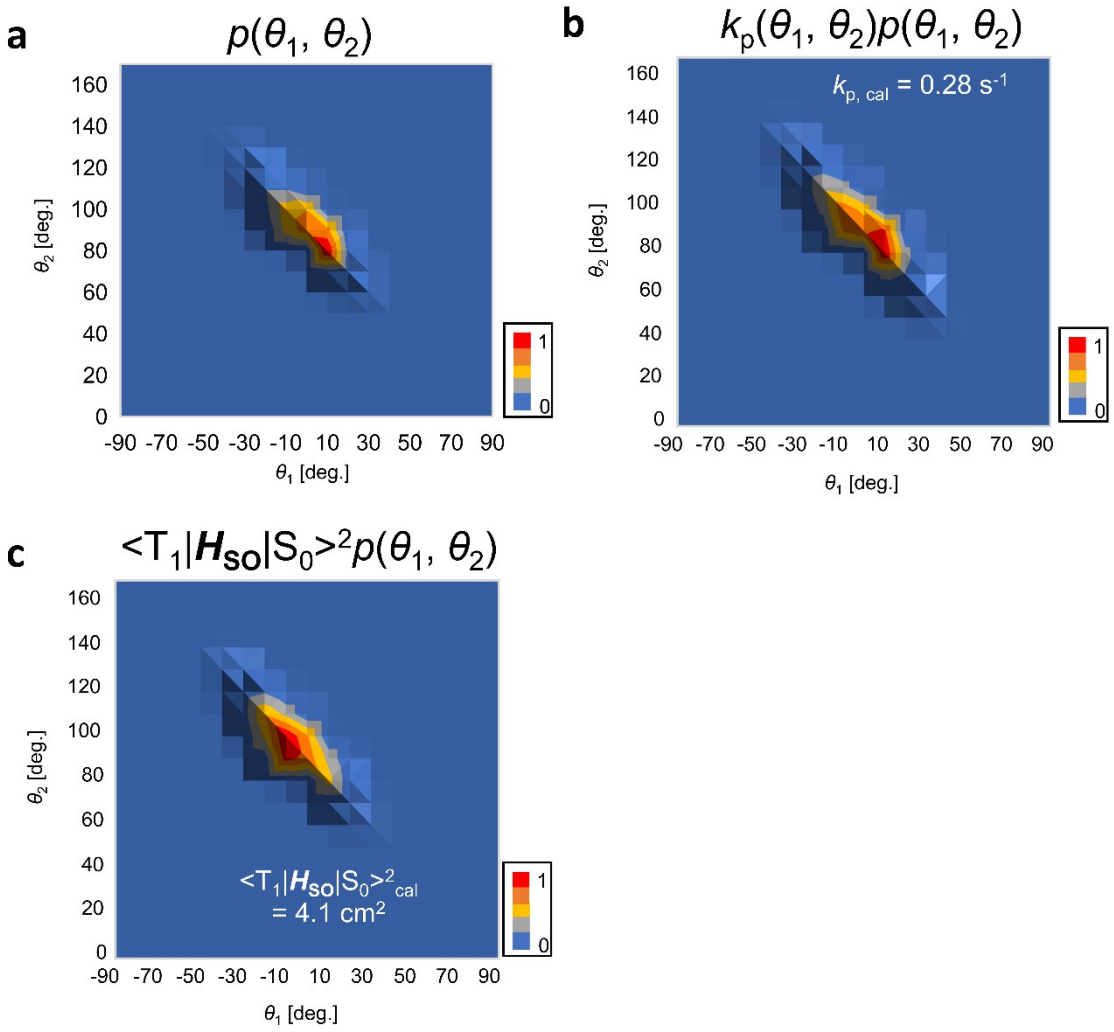

Fig. S19. Histograms of $p(\theta_1, \theta_2)$ (a), $k_p(\theta_1, \theta_2)p(\theta_1, \theta_2)$ (b), and $\langle T_1|\boldsymbol{H}_{SO}|S_0\rangle^2 p(\theta_1, \theta_2)$ (c) in models where $\Delta E(\theta_1, \theta_2)$ at **3h** increases 8-fold for a solid crystalline host compared with vacuum condition.

12. Supporting Reference

S1. K. Fukasawa, Y. Sugawara, R. Tsuru, T. Yamashita and S. Hirata, *J. Phys. Chem. Lett.*, 2022, **13**, 7788.

S2. S. Hirata, K. Totani, J. Zhang, T. Yamashita, H. Kaji, S. R. Marder, T. Watanabe, and C. Adachi, *Adv. Funct. Mater.*, 2013, **23**, 3386–3397.

S3. S. Hirata, *Appl. Phys. Rev.*, 2022, **9**, 011304.

S4. F. Xiao, H. Gao, Y. Lei, W. Dai, M. Liu, X. Zheng, Z. Cai, X. Huang, H. Wu and D. Ding, *Nat. Commun.*, 2022, **13**, 186.

S5. B. Chen, W. Huang, X. Nie, F. Liao, H. Miao, X. Zhang and G. Zhang, *Angew. Chem. Int. Ed.*, 2021, **60,** 16970-16973.

S6. D. Li, J. Yang, M. Fang, B. Z. Tang and Z. Li, *Sci. Adv.*, 2022, **8**, eabl8392.

S7. J. Jovaišaitė, S. Kirschner, S. Raišys, G. Kreiza, P. Baronas, S. Juršėnas and M. Wagner, *Angew. Chem. Int. Ed.*, 2023, **62**, e202215071.

S8. X. Shen, Y. Luo, K. Chen, C. Fu, R. Liu, Y. Huang, K. Wu, J. Luoa and Z. Lu, *Chem. Commun.*, 2023, **59**, 7036-7039.

S9. X. Zheng, Q. Han, Q. Lin, C. Li, J. Jiang, Q. Guo, X. Ye, W. Z. Yuan, Y. Liu and X. Tao., *Mater. Horiz.*, 2023, **10**, 197-208.

S10. B. Sk and S. Hirata, *Adv. Sci.*, 2024, **11**, 2308897.

S11. I. Bhattacharjee, S. Hirata, *Adv. Mater.*, 2000, **32**, 2001348.

S12. R. Huang, J. Avó, T. Northey, E. Chaning-Pearce, J. L. dos Santos, J. S. Ward, P. Data, M. K. Etherington, M. A. Fox, T. J. Penfold, M. N. Berberan Santos, J. C. Lima, M. R. Bryce and F. B. Dias, *J. Mater. Chem. C*, 2017, **5**, 6269–6280.

S13. S. Hirata, M. Nishio, H. Uchida, T. Usuki, T. Nakae, M. Miyachi, Y. Yamano and H. Nishihara, *J. Phys. Chem. C*, 2020, **124**, 3277-3286.

S14. J. K. Hurley, N. Sinai and H. Linschitz, *J. Photochem. Photobiology*, 1983, **38**, 9-14.

S15. T. Kamatsuki, I. Bhattacharjee and S. Hirata, *J. Phys. Chem. Lett.*, 2020, **11**, 8675-8681.

S16. E. H. Badriyah, K. Hayashi, B. Sk, R. Takano, T. Ishida and S. Hirata, *Adv. Sci.*, 2023, **10**, 2304374.

S17. S. Hirata and I. Bhattacharjee, *J. Phys. Chem. A*, 2021, **125**, 885–894.

S18. I. Bhattacharjee, K. Hayashi and S. Hirata, *JACS Au*, 2021, **1**, 945-954.

S19. K. Mori, T. P. M. Goumans, E. van Lenthe and F. Wang, *Phys. Chem. Chem. Phys.* 2014, **16**, 14523.